

Higher harmonics in planar Hall effect induced by cluster magnetic multipoles

Received: 13 June 2022

Accepted: 13 October 2022

Published online: 30 October 2022

 Check for updates

Jeongkeun Song^{1,2}, Taekoo Oh^{1,2,3}, Eun Kyo Ko^{1,2}, Ji Hye Lee^{1,2},
Woo Jin Kim^{4,5}, Yangyu Zhu⁶, Bohm-Jung Yang^{1,2,3}, Yangyang Li⁶ ✉ &
Tae Won Noh^{1,2} ✉

Antiferromagnetic (AFM) materials are attracting tremendous attention due to their spintronic applications and associated novel topological phenomena. However, detecting and identifying the spin configurations in AFM materials are quite challenging due to the absence of net magnetization. Herein, we report the practicality of utilizing the planar Hall effect (PHE) to detect and distinguish “cluster magnetic multipoles” in AFM Nd₂Ir₂O₇ (NIO-227) fully strained films. By imposing compressive strain on the spin structure of NIO-227, we artificially induced cluster magnetic multipoles, namely dipoles and A₂- and T₁-octupoles. Importantly, under magnetic field rotation, each magnetic multipole exhibits distinctive harmonics of the PHE oscillation. Moreover, the planar Hall conductivity has a nonlinear magnetic field dependence, which can be attributed to the magnetic response of the cluster magnetic octupoles. Our work provides a strategy for identifying cluster magnetic multipoles in AFM systems and would promote octupole-based AFM spintronics.

Antiferromagnetic (AFM) materials have attracted considerable interest as promising materials for next-generation spintronics^{1–5} and novel topological phenomena^{6–11}. This interest is largely due to the fact that the AFM spin arrangement produces zero net magnetization, leading to an absence of stray fields and insensitivity to external magnetic fields^{12,13}. Additionally, the spin precession for AFM order is much faster than that in ferromagnets¹⁴. The resonance frequencies in antiferromagnets are in the terahertz range^{15–17}, whereas those of ferromagnets are in the gigahertz range. In parallel with AFM spintronics, antiferromagnets with topologically protected states have become another focus of recent interest. As AFM spin order breaks the time-reversal symmetry (TRS) or inversion symmetry, various topologically nontrivial states including the Weyl semimetal^{6–8}, axion insulator^{9,10}, and Möbius insulator¹¹ can theoretically emerge.

To develop novel AFM spintronics and investigate topological states in AFM materials, understanding the relationship between the

spin texture and emergent phenomena in AFM materials is essential. This relationship can be theoretically described by the recently introduced cluster multipole theory (CMT)¹⁸. In CMT¹⁸, magnetic structures are classified as “cluster multipoles” (dipole and additional high-rank multipoles) according to irreducible representations of the crystallographic point group. These cluster multipoles can be regarded as order parameters that reflect symmetry breaking in AFM materials. In particular, some cluster magnetic octupole (CMO) (i.e., T₁ octupole) belongs to the same magnetic point group (–42m') as the magnetic dipole¹⁸, leading to symmetry breaking and generating nonvanishing Berry curvature. In fact, the analysis using CMOs has been recently extended to understanding the large response of AHE^{18–21}, magneto-optical signals²², the SHE^{23–25}, the anomalous Nernst effect^{26–28}, and perpendicular magnetization^{29,30} in AFM materials. However, due to the absence of net magnetization, experimental identification of the CMOs in AFM materials is very challenging. To date, it has been limited

¹Center for Correlated Electron Systems, Institute for Basic Science (IBS), Seoul 08826, Korea. ²Department of Physics and Astronomy, Seoul National University, Seoul 08826, Korea. ³Center for Theoretical Physics (CTP), Seoul National University, Seoul 08826, Korea. ⁴Stanford Institute for Materials and Energy Sciences, SLAC National Accelerator Laboratory, Menlo Park, CA 94025, USA. ⁵Department of Applied Physics, Stanford University, Stanford, CA 94305, USA. ⁶School of Physics, Shandong University, Jinan 250100, China. ✉e-mail: yangyang.li@sdu.edu.cn; twnoh@snu.ac.kr

to X-ray magnetic circular dichroism measurements³¹ and the neutron scattering technique³².

The planar Hall effect (PHE) has been considered a method of probing the physical properties of materials such as magnetism and topology. The PHE corresponds to the development of a Hall voltage when electric and magnetic fields are coplanar, which is different from the usual Hall effect where they are perpendicular to each other. Initially, the PHE was observed in ferromagnetic systems^{33–36}, detecting the anisotropic magnetization of ferromagnetic materials. Additionally, the PHE has recently been in the spotlight due to its role in detecting topological characteristics such as the chirality arising from Weyl fermions in magnetic Weyl semimetals^{37–40}. The associated PHE in both ferromagnets and Weyl semimetals exhibit $\sin(2\phi)$ or second harmonic PHE oscillations. In contrast, higher harmonics PHE oscillations beyond second in topological systems^{41–44} have been recently reported, in which higher harmonics PHE originated from additional unknown parameters in materials.

Among many kinds of AFM materials, the family of $5d$ AFM materials $R_2\text{Ir}_2\text{O}_7$ (R : rare-earth ions: Eu, Y, Nd, and Pr) has received considerable attention due to a plethora of intriguing properties^{6,7}. The crystal structure of NIO-227 is composed of Ir and Nd tetrahedral sublattices (Fig. 1a), which have a symmetry identical to that of the diamond lattice. Most $R_2\text{Ir}_2\text{O}_7$ bulk compounds exhibit an intriguing spin configuration called all-in-all-out (AIAO). According to CMT, the AIAO ordering of bulk $R_2\text{Ir}_2\text{O}_7$ is equivalent to the A_2 -CMO^{21,45}. This A_2 -CMO breaks the TRS and generates nonvanishing Berry curvature, resulting in topological properties in momentum space such as the magnetic Weyl semimetal⁶ and Axion insulator⁶.

Here, we demonstrate the detection and identification of CMO in fully-strained AFM $\text{Nd}_2\text{Ir}_2\text{O}_7$ (NIO-227) film via the PHE. Under epitaxial strain, three kinds of cluster multipoles (dipoles and A_2 - and T_1 -CMOs) can be induced in the NIO-227 film. By rotating the magnetic field, distinctive harmonics in the PHE oscillation were observed. Specifically, the dipole induces the second harmonic due to longitudinal magnetization (Fig. 1c), whereas the A_2 - and T_1 -CMO induce fourth and sixth harmonics in the PHE oscillation, respectively. We demonstrate that the higher harmonics of the PHE oscillation for both CMOs originate from the magnetic response of the CMOs, called orthogonal magnetization (OM) (Fig. 1d). Furthermore, cluster multipoles induce nonlinear magnetic field-dependent the planar Hall conductivity. This nonlinear magnetic field behavior of the planar Hall conductivity can be understood in terms of the magnetic properties of the cluster magnetic dipole and CMOs.

Results

To investigate the magnetotransport properties of CMOs, we fabricated 15 nm fully strained NIO-227 films on a (111)-oriented yttria-stabilized zirconia (YSZ) substrate. More details on the growth are provided in the Methods section. Figure 2a shows the X-ray diffraction (XRD) pattern of a (111)-oriented NIO-227 thin film on a YSZ substrate. The strong odd-pair peaks in the XRD pattern exhibit excellent crystallization of the pyrochlore phase in the NIO film. Further analysis of the reciprocal space map (Fig. 2b) shows that the NIO-227 film is fully strained with a compressive strain of $\sim 1\%$. As mentioned earlier, the presence of compressive strain in the NIO-227 film is crucial, as it modulates the AIAO ordering and develops T_1 -CMOs. Figure 2c shows

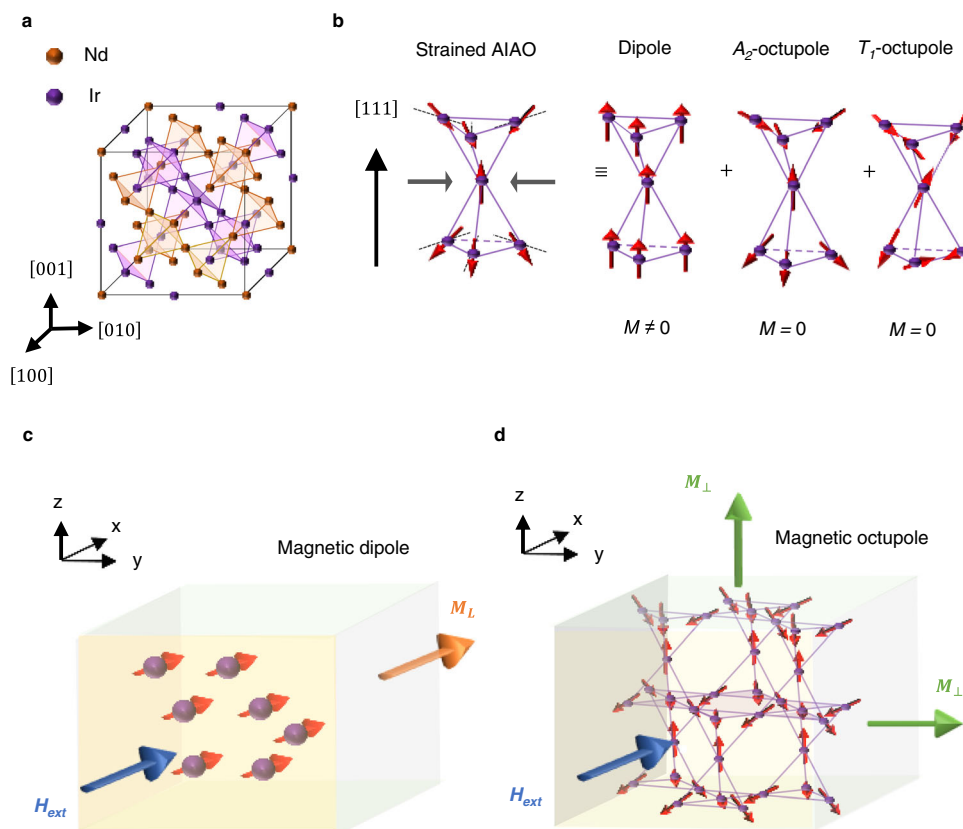


Fig. 1 | Schematic diagram of strain-induced cluster magnetic multipoles and OM in $\text{Nd}_2\text{Ir}_2\text{O}_7$ thin films. **a** Schematic view of the pyrochlore lattice structure of $\text{Nd}_2\text{Ir}_2\text{O}_7$. **b** When compressive strain is applied to $\text{Nd}_2\text{Ir}_2\text{O}_7$ along the [111] direction, the AIAO configuration of the magnetic spin experiences spin canting. Such canting can be represented by three distinctive magnetic multipoles (dipole, A_2 -octupole, and T_1 -octupole). Note that the dipole has finite magnetization, whereas

the A_2 -octupole and T_1 -octupole do not have magnetization. **c** Schematic diagram of the longitudinal magnetization induced by the dipole. When H_{ext} is applied along the x - y plane, the spin direction is aligned in the direction of H_{ext} . **d** Schematic diagram of the OM induced by coupling between an external magnetic field (H_{ext}) and magnetic octupoles. The OM can be induced in two directions: normal to the surface and in-plane.

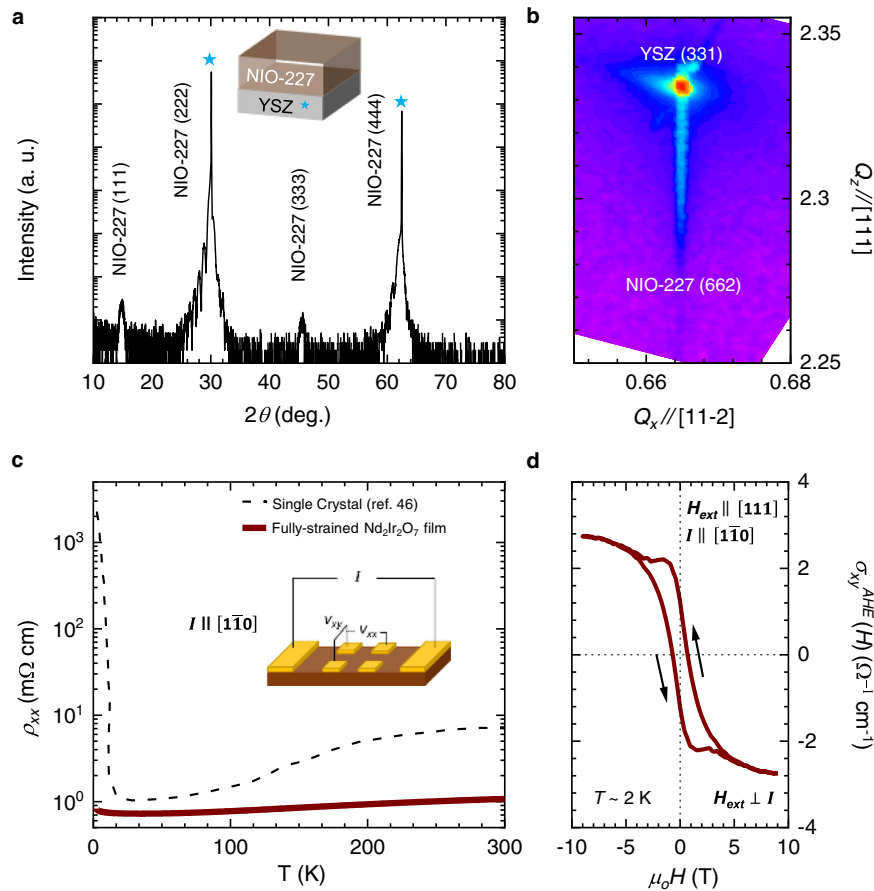


Fig. 2 | Characterization of a $\text{Nd}_2\text{Ir}_2\text{O}_7$ thin film. **a** High-resolution XRD pattern of a 15 nm thick $\text{Nd}_2\text{Ir}_2\text{O}_7$ (NIO-227) thin film. The NIO-227 thin film was grown on a YSZ substrate. **b** Reciprocal space map of the NIO-227 film in the vicinity of the YSZ (331) reflection, indicating that the NIO-227 film is fully strained. **c** The plot of the longitudinal resistivity, ρ_{xx} , vs. temperature, T , of NIO-227 thin film and single

crystal (ref. 46 in the main manuscript). **d** The AHE is measured by applying H_{ext} along the [111] direction and I along the $[\bar{1}\bar{1}0]$ direction at 2 K. A clear AHE without a magnetic field is the signature of the presence of the T_1 -octupole in the NIO-227 thin film.

the longitudinal resistivity $\rho_{xx}(T)$ of the NIO-227 thin film as a function of temperature without a magnetic field. Clearly, with decreasing T , the NIO-227 film exhibits stronger semimetallic behavior than that of bulk NIO-227. At $T \sim 2$ K, our NIO-227 film has a ρ_{xx} of ~ 2.28 m Ω cm, whereas that of bulk NIO-227 is $\sim 2.20 \times 10^3$ m Ω cm⁴⁶. With compressive strain, the valence and conduction bands move in the NIO-227 film. The valence and conduction bands cross near the Fermi level, resulting in the development of electron and hole pockets²¹. These previous model calculations explain the enhancement of the conductivity in the NIO-227 thin film compared to the bulk.

Moreover, the AHE ($\sigma_{xy}^{\text{AHE}}(H)$) of the NIO-227 film was measured with H_{ext} applied along the [111] direction below 30 K. As shown in Fig. 2d, $\sigma_{xy}^{\text{AHE}}(H)$ at 2 K shows a hysteric feature with a finite value at 0 T, known as the spontaneous Hall effect²¹. In our strained NIO-227 thin film, the AHE and spontaneous Hall effect developed below 30 and 15 K, respectively. The value of the spontaneous Hall effect approached the maximum value at 2 K. More details are provided in Supplementary Materials (Supplementary Fig. 1 and Note 1). The appearance of AHE below 30 K was previously attributed to Ir spin ordering²¹. In contrast, the emergence of the spontaneous Hall effect without magnetization below 15 K in the NIO-227 film is known to be the nontrivial contribution of the T_1 -CMO to the Berry curvature²¹, which is amplified by Nd ordering through f - d exchange interaction. The effect of Nd ordering can give an additional hysteric component on AHE²¹ (Supplementary Fig. 2). In our 15 nm NIO-227 film, the spontaneous Hall effect is observed without magnetization, which is induced by T_1 -CMO in the film (Supplementary Fig. 1c).

To detect CMOs in the NIO-227 film, we performed PHE measurements. As shown in Fig. 3a, the PHE ($\Delta\sigma_{xy}^{\text{PHE}}(\phi, H = \pm 9$ T)) below 30 K was measured across the width of the sample by applying I along the $[\bar{1}\bar{1}0]$ direction with the rotation of H_{ext} . The details about the experimental measurement and data process are provided in the “Methods” and Supplementary Materials (Supplementary Fig. 3 and Note 2), respectively. In the range of 15–30 K, the $\Delta\sigma_{xy}^{\text{PHE}}(\phi)$ curves in the NIO-227 film mostly exhibit $\sin(2\phi)$ oscillations (Fig. 3b). The $\sin(2\phi)$ behavior (second harmonic) of the $\Delta\sigma_{xy}^{\text{PHE}}(\phi)$ oscillation above 15 K can be understood as the magnetization from dipolar order. As shown in Fig. 1b, the NIO-227 film has a cluster dipole, which can be regarded as ferromagnetic ordering. This cluster dipole induces M_L to be directed along H_{ext} , which can result in the second harmonic of the $\Delta\sigma_{xy}^{\text{PHE}}(\phi)$ oscillation. Thus, the second harmonic of the $\Delta\sigma_{xy}^{\text{PHE}}(\phi)$ oscillation above 15 K can be understood as the transverse voltage developed by the cluster dipole in the NIO-227 film under H_{ext} .

Below $T < 15$ K, the behavior of the $\Delta\sigma_{xy}^{\text{PHE}}(\phi)$ curves are complex but periodic, exhibiting oscillations of multiple harmonics. As shown in Fig. 3b, the $\Delta\sigma_{xy}^{\text{PHE}}(\phi)$ oscillation at 2 K cannot be explained only by the typical second harmonic induced by dipolar order. Such complex behavior of the $\Delta\sigma_{xy}^{\text{PHE}}(\phi)$ oscillation can be seen in the contour plot presented in Fig. 3c. Whereas the second harmonic of $\Delta\sigma_{xy}^{\text{PHE}}(\phi)$ (green region) exists in all temperature regions below 30 K, additional harmonics (red region) of the $\Delta\sigma_{xy}^{\text{PHE}}(\phi)$ oscillation appears below 15 K. As a result, the $\Delta\sigma_{xy}^{\text{PHE}}(\phi)$ curve exhibits oscillations of multiple harmonics below 15 K.

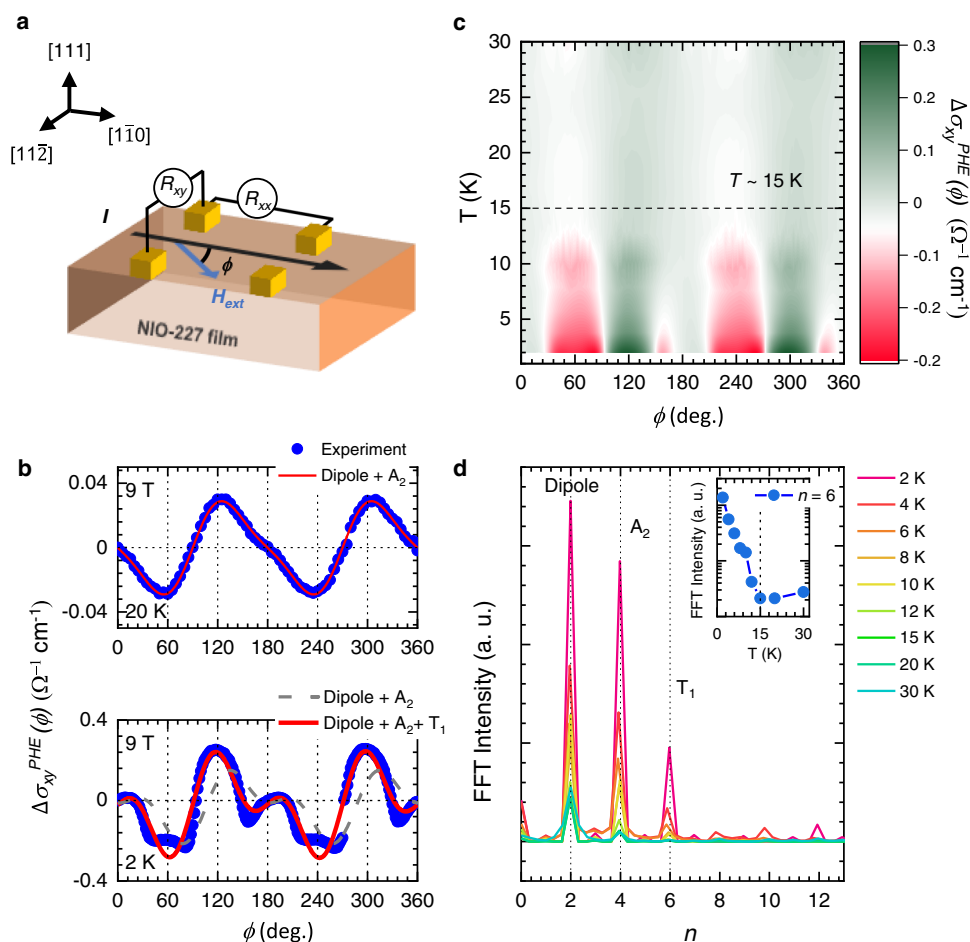


Fig. 3 | Anomalous magnetic oscillation in the $\Delta\sigma_{xy}^{\text{PHE}}(\phi, H = \pm 9 \text{ T})$ of the NIO-227 thin film. **a** Schematic diagram of the $\Delta\sigma_{xy}^{\text{PHE}}(\phi)$ measurement geometry. In this geometry, I is applied along the $[1\bar{1}0]$ direction and H_{ext} is rotated within the sample plane. **b** $\Delta\sigma_{xy}^{\text{PHE}}(\phi)$ curves at 20 and 2 K. At 20 K, the $\Delta\sigma_{xy}^{\text{PHE}}(\phi)$ curve has a $\sin(2\phi)$ oscillation. At 2 K, the $\Delta\sigma_{xy}^{\text{PHE}}(\phi)$ curve has an inhomogeneous oscillation, indicating a hidden magnetic origin. **c** Contour plot of all $\Delta\sigma_{xy}^{\text{PHE}}(\phi)$ curves below 30 K. A gradual appearance of the abovementioned peaks can be seen (red region). While

the peaks at $\phi = 120^\circ$ and 300° (green region) exist above $T = 15 \text{ K}$, the peaks near $\phi = 60^\circ, 180^\circ, 240^\circ,$ and 340° (red region) appear below $T = 15 \text{ K}$. **d** FFT results of all $\Delta\sigma_{xy}^{\text{PHE}}(\phi)$ curves with different T . The FFT intensities of the second, fourth, and sixth harmonics are related to magnetization from the dipole, OM induced by the A_2 -CMO, and OM induced by the T_1 -CMO, respectively. The inset shows the temperature dependence of the sixth harmonic below 30 K. Clearly, the sixth harmonic order emerges at 15 K, which indicates the role of the T_1 -CMO.

To obtain further insight into the anomalous behavior of $\Delta\sigma_{xy}^{\text{PHE}}(\phi)$ curves below 15 K, we performed a fast Fourier transform (FFT) of the measured $\Delta\sigma_{xy}^{\text{PHE}}(\phi)$ curves. The detailed FFT procedure is provided in Supplementary Materials (Supplementary Fig. 4). The harmonics (n) dependency of the FFT intensity in the $\Delta\sigma_{xy}^{\text{PHE}}(\phi)$ oscillation is shown in Fig. 3d. At 30 K, the second harmonic always exists, which is induced by the cluster dipole. The additional higher harmonics appear below 30 K. The appearance of the fourth harmonic in the $\Delta\sigma_{xy}^{\text{PHE}}(\phi)$ oscillation has been attributed to the A_2 -CMO-induced chiral anomaly in $\text{Pr}_2\text{Ir}_2\text{O}_7$ thin films⁴¹. Considering that both $\text{Pr}_2\text{Ir}_2\text{O}_7$ and NIO-227 films have the A_2 -CMO, the observed fourth harmonic of the $\Delta\sigma_{xy}^{\text{PHE}}(\phi)$ oscillation in the NIO-227 film should originate from the A_2 -CMO. However, the appearance of the sixth harmonic below 15 K (inset in Fig. 3d) cannot be explained by either the dipole or A_2 -CMO.

To elucidate the appearance of the sixth harmonic in the $\Delta\sigma_{xy}^{\text{PHE}}(\phi)$ oscillation, we calculate $\Delta\sigma_{xy}^{\text{PHE}}$ from the dipole and A_2 - and T_1 -CMOs using the phenomenological model. Notably, the A_2 -CMO induces an unusual magnetic response perpendicular to H_{ext} . This magnetic response was initially observed in a $\text{Eu}_2\text{Ir}_2\text{O}_7$ single crystal by torque magnetometry and defined as OM³⁰. As mentioned above, the T_1 -CMO is also expected to exhibit OM. Employing the expression³⁰ of the OM in $\text{Eu}_2\text{Ir}_2\text{O}_7$, we obtained the ϕ dependence of $\Delta\sigma_{xy}^{\text{PHE}}(\phi)$ for our system,

expressed as follows:

$$\Delta\sigma_{xy}^{\text{PHE}}(\phi) = \sigma_{xy}^{\text{Dipole}} + \sigma_{xy}^{A_2} + \sigma_{xy}^{T_1} = A\sin(2\phi) + B\sin(4\phi) + C\sin(6\phi) \quad (1)$$

where A is the PHE coefficient of the dipole. B and C are the PHE coefficients of the OM induced by A_2 - and T_1 -CMOs, respectively. The detailed theoretical calculation is discussed in Supplementary Materials (Supplementary Figs. 5 and 6, and Note 3): Then, Eq. (1) can explain the appearance of peaks of the second, fourth, and sixth harmonics (Fig. 3d) by the M_L induced by the dipole, OM induced by the A_2 -CMO, and OM induced by the T_1 -CMO, respectively. In the range of 15–30 K, the $\Delta\sigma_{xy}^{\text{PHE}}(\phi)$ oscillation can be fitted with the M_L and OM induced by the dipole and A_2 -CMO, respectively. The fitting of the $\Delta\sigma_{xy}^{\text{PHE}}(\phi)$ oscillation at 20 K without the $\sin(6\phi)$ term in Eq. (1) is shown in Fig. 3b. This indicates that the cluster dipole and A_2 -CMO of Ir spin ordering induce second and fourth harmonics of the $\Delta\sigma_{xy}^{\text{PHE}}(\phi)$ oscillation, respectively, while the contribution of the T_1 -CMO is small in this temperature region.

In contrast, the $\Delta\sigma_{xy}^{\text{PHE}}(\phi)$ oscillation below 15 K can only be fitted by including the T_1 -CMO contribution. As shown in Fig. 3b, Eq. (1), by including the $\sin(6\phi)$ term from the T_1 -CMO (red), well fits $\Delta\sigma_{xy}^{\text{PHE}}(\phi)$ at

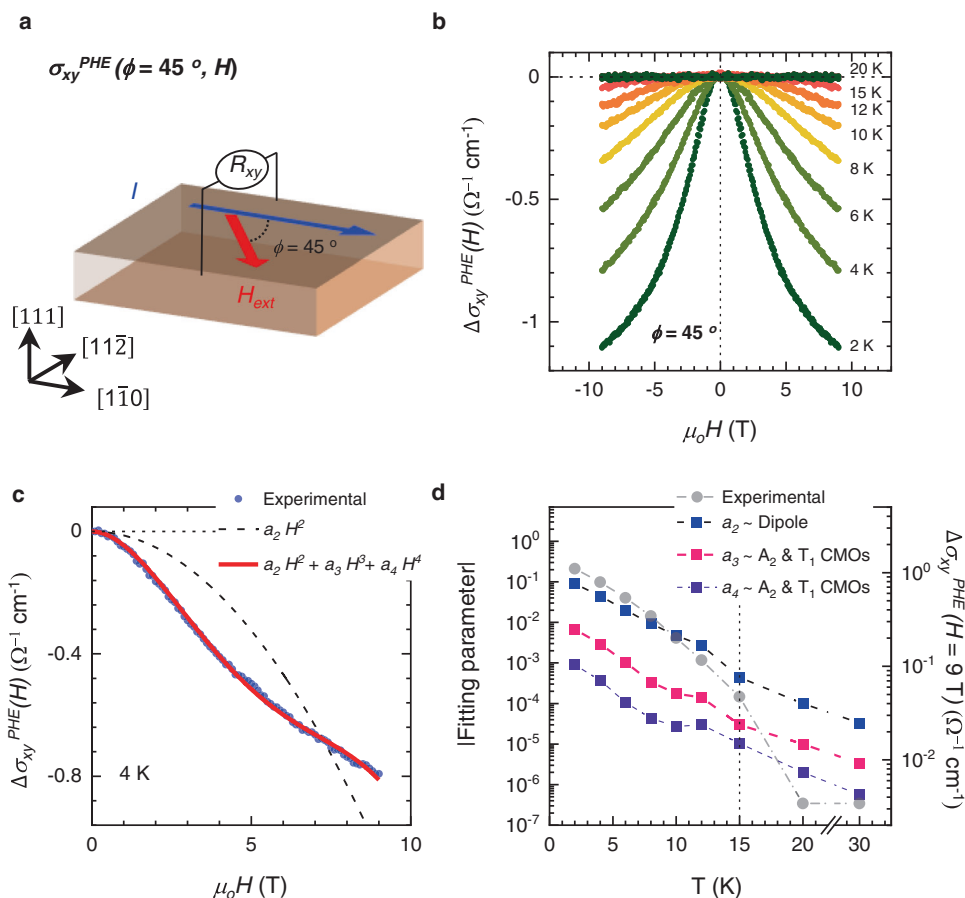


Fig. 4 | Nonlinear magnetic behavior of the $\Delta\sigma_{xy}^{\text{PHE}}(\phi = 45^\circ, H)$ of the NIO-227 thin film. **a** Schematic diagram of the $\Delta\sigma_{xy}^{\text{PHE}}(H)$ measurement geometry. In this geometry, the angle between the current and magnetic field (± 9 T) is 45° . Surprisingly, $\Delta\sigma_{xy}^{\text{PHE}}(H)$ shows H_{ext} dependency below $T = 15$ K due to OM. **b** $\Delta\sigma_{xy}^{\text{PHE}}(H)$ curves as a function of H_{ext} below $T = 20$ K. In the region of $15 \text{ K} < T < 20$ K, the value of $\Delta\sigma_{xy}^{\text{PHE}}(H)$ is nearly zero. The slight deviation of $\Delta\sigma_{xy}^{\text{PHE}}(H)$ near $H_{\text{ext}} = \pm 9$ T at $T = 15$ K is possibly due to dipolar order. **c** Logarithmic plot of the results of fitting $\Delta\sigma_{xy}^{\text{PHE}}(H)$ at $T = 4$ K

with $\Delta\sigma_{xy}^{\text{PHE}}(H) = a_2H^2 + a_3H^3 + a_4H^4$ (red line). The a_2 , a_3 , and a_4 terms correspond to longitudinal magnetization, OM from the A_2 -CMO, and OM from the T_1 -CMO, respectively. Note that without the a_3 and a_4 contributions (black dashed line), the experimental data (blue dots) do not fit well, indicating the role of OM induced by both the A_2 - and T_1 -octupoles. **d** The plot of extracted fitting parameters a_2 , a_3 , and a_4 and $\Delta\sigma_{xy}^{\text{PHE}}(H = 9 \text{ T})$ for the measured T .

2 K. The fitting results of $\Delta\sigma_{xy}^{\text{PHE}}(\phi)$ for measured temperature using Eq. (1) is provided in the Supplementary Materials (Supplementary Fig. 7). The temperature dependence of the fitting result is consistent with the appearance of the sixth harmonic peak below 15 K in the NIO-227 film. Furthermore, a similar temperature characteristic of T_1 -CMOs is observed in not only AHE but also in anisotropic magnetoconductivity and out-of-plane rotation magnetoconductivity (Supplementary Figs. 8 and 9). The multiple harmonics of anisotropic magnetoconductivity and out-of-plane rotation magnetoconductivity are developed below 15 K. These complex behaviors can be explained by including the contribution of T_1 -CMOs, which is amplified by Nd ordering through f - d exchange interaction²¹. Therefore, we can confirm that the higher harmonics of $\Delta\sigma_{xy}^{\text{PHE}}(\phi)$ originate from A_2 - and T_1 -CMOs via OM.

Since the OM is the coupling effect between CMOs and H_{ext} and is known to have an H -field dependence³⁰, the $\sigma_{xy}^{\text{PHE}}(H)$ of NIO-227 should exhibit behavior different from that of a ferromagnet. We measured $\Delta\sigma_{xy}^{\text{PHE}}(\phi = 45^\circ, H)$ below 30 K by fixing $\phi = 45^\circ$ between I and H_{ext} (Fig. 4a). R_{xx} and R_{xy} were simultaneously measured and symmetrized, and $\Delta\sigma_{xy}^{\text{PHE}}(H)$ was obtained (Supplementary Fig. 10). The $\Delta\sigma_{xy}^{\text{PHE}}(H)$ curves with respect to H_{ext} below 20 K are shown in Fig. 4b. In the range of 15–20 K, the values of the $\Delta\sigma_{xy}^{\text{PHE}}(H)$ curves remain near zero at $H_{\text{ext}} = +9$ and -9 T. However, below 15 K, the values of the $\Delta\sigma_{xy}^{\text{PHE}}(H)$ curves have finite values with increasing H_{ext} and reach $\Delta\sigma_{xy}^{\text{PHE}}(H) = +9\text{T} - 1.103 \text{ } \Omega^{-1} \text{ cm}^{-1}$ at 2 K.

By considering the OM induced by the A_2 -CMO and T_1 -CMO, we calculated $\Delta\sigma_{xy}^{\text{PHE}}(H)$ using the phenomenological model. Based on our calculations, the relation of $\Delta\sigma_{xy}^{\text{PHE}}(H)$ to H_{ext} can be expressed as follows:

$$\Delta\sigma_{xy}^{\text{PHE}}(H) = a_2H^2 + a_3H^3 + a_4H^4 \quad (2)$$

where a_2 is the coefficient of longitudinal magnetization induced by the dipole. Both a_3 and a_4 are the coefficients of OM induced by A_2 - and T_1 -CMOs. The details about the data process and theoretical calculation are provided in Supplementary Materials (Supplementary Note 4). Figure 4c shows the fitting results for $\Delta\sigma_{xy}^{\text{PHE}}(H)$ at a selected temperature of ~ 4 K with (red line) and without (black dashed line) the H^3 and H^4 terms. Note that the exact proportions of dipole and CMOs cannot be determined by experimental PHE due to the complexity behind transport phenomena⁴¹, but we can get it theoretically (Supplementary Fig. 11). The fitting with the OM contribution explains the experimental results better than that with the dipole, demonstrating the development of OM from H_{ext} . Additionally, all measured $\Delta\sigma_{xy}^{\text{PHE}}(H)$ values below 20 K are well fitted by Eq. (2) (Supplementary Fig. 12). The contribution of the PHE coefficients of a_2 , a_3 , and a_4 to $\Delta\sigma_{xy}^{\text{PHE}}(H)$ below 30 K is shown in Fig. 4d. Below 30 K, the dipole induces an H^2 dependence of $\Delta\sigma_{xy}^{\text{PHE}}(H)$ due to the longitudinal magnetization, as shown in Fig. 1c. In contrast, below 15 K, the contributions of a_2 , a_3 , and a_4 coexist. While dipolar order still affects $\Delta\sigma_{xy}^{\text{PHE}}(H)$, a_3 and a_4 may

appear due to the OM induced by both the A_2 and T_1 -CMOs. Through theoretical analysis and the PHE results, we confirm that the anomalous behavior of the PHE indeed originates from A_2 - and T_1 -CMOs. Our results summarizing the contributions to the AHE and PHE of the cluster magnetic dipole, A_2 -CMO, and T_1 -CMO are shown in Table 1 in the Supplementary Materials.

Discussion

In summary, the PHE of the AFM NIO-227 film exhibits unique features different from those of ferromagnetic materials. The CMOs without magnetization affect the PHE, resulting in higher harmonics of the PHE oscillation beyond the second harmonic. Notably, A_2 - and T_1 -CMOs produce fourth and sixth harmonics of PHE oscillations, respectively. This feature of CMOs can be well explained by considering the magnetic characteristic of CMOs called OM in our theoretical calculations. Moreover, the OM of CMOs shows an intriguing H_{ext} dependency, which induces the nonlinear PHE when the angle between H_{ext} and I is 45° .

We would like to make some remarks about the CMOs in AFM materials. According to recent theoretical studies and experiments on antiferromagnets, the magnetic octupole is crucial for stabilizing Weyl fermions near the Fermi energy^{18,27,47–51} and inventing magnetic field-free switching spintronic devices^{23–25,48–50}. Moreover, AHE, SHE, and Nernst effects have been experimentally observed in Kagome antiferromagnets^{19,20,25,26,29}, in which magnetic structure can also be classified with CMO¹⁸. Therefore, understanding and manipulating the CMOs are thus important to achieve novel topological phases and physics in AFM systems. However, due to the absence of magnetization, detection and characterization of CMOs and multipoles beyond dipoles have been difficult. In this context, our strategy to distinguish A_2 - and T_1 -CMOs could be extensively used to detect and identify cluster multipoles^{18,45} via the PHE. Thus, our work paves the way for detecting and identifying AFM order, which is expected to facilitate the development of novel functionalities using AFM materials.

Methods

Film fabrication and structural characterization

Fully strained NIO-227 films were grown in situ on insulating YSZ substrates using the “repeated rapid high-temperature synthesis epitaxy” (RRHSE) method²¹. This film growth method is a modified form of pulsed laser deposition, in which repetitive short-term thermal annealing processes are conducted using an infrared laser. The RRHSE consists of two key steps completed in one thermal cycle. In the first step, amorphous stoichiometric NIO-227 and compensational IrO_2 layers are deposited with a KrF excimer laser ($\lambda = 248 \text{ nm}$, 5 Hz) at $T \sim 600^\circ\text{C}$ and $P_{\text{O}_2} \sim 50 \text{ mTorr}$. During the second step, the pyrochlore phase is formed by rapidly raising T to 850°C at a rate of $\sim 400^\circ\text{C min}^{-1}$, and the sample is exposed to the high T for a sufficient period. We repeated the deposition and thermal synthesis processes until the desired film thickness was obtained.

Transport and magnetic properties

Magnetotransport properties were measured via a standard four-point probe method using a commercial physical property measurement system (PPMS; Quantum Design Inc., San Diego, CA, USA), which has a base T of 2 K and a maximum magnetic field of 9 T . Au layer (thickness: $\sim 50 \text{ nm}$) was deposited by an e-beam evaporator on the NIO-227 film and used as an electrode. For the AHE measurement, the current was applied along the $[\bar{1}10]$ direction, while H was applied in the $[111]$ direction. For the PHE measurement, the current was applied along the $[\bar{1}10]$ direction and H was rotated between the $[\bar{1}10]$ and $[11\bar{2}]$ directions. The R_{xy} and longitudinal magnetoresistance R_{xx} below 30 K were simultaneously measured while varying ϕ and fixing H_{ext} at $\pm T$. The out-of-plane contribution of H_{ext} caused by a slight misalignment of

the electrode can be removed by symmetrizing the R_{xy} acquired at $+9$ and -9 T . Then, the planar Hall conductivity σ_{xy}^{PHE} is calculated by $\sigma_{xy}^{\text{PHE}} = \frac{-\rho_{xy}^{\text{PHE}}}{\rho_{xy}^{\text{PHE}^2} + \rho_{xx}^2}$ and normalized ($\Delta\sigma_{xy}^{\text{PHE}}(\phi)$); here, $-\rho_{xy}^{\text{PHE}}$ and ρ_{xx} are the PHE resistivity and longitudinal resistivity, respectively. The detailed symmetrization process of the PHE is provided in Supplementary Materials (Supplementary Fig. 3).

Data availability

All relevant data presented in this manuscript are available from the authors upon reasonable request. The source data underlying Figs. 2, 3b, c, d, 4b, and Supplementary Fig. 8 are provided as a Source Data file. Source data are provided with this paper.

References

- Shick, A. B. et al. Spin-orbit coupling induced anisotropy effects in bimetallic antiferromagnets: A route towards antiferromagnetic spintronics. *Phys. Rev. B* **81**, 212409 (2010).
- MacDonald, A. H. & Tsoi, M. Antiferromagnetic metal spintronics. *Philos. Trans. R. Soc. A* **369**, 3098–3114 (2011).
- Gomonay, E. V. & Loktev, V. M. Spintronics of antiferromagnetic systems. *Low. Temp. Phys.* **40**, 17–35 (2014).
- Gomonay, O., Jungwirth, T. & Sinova, J. Concepts of antiferromagnetic spintronics. *Phys. Stat. Sol. Rrl.* **11**, 1700022 (2017).
- Jungwirth, T., Marti, X., Wadley, P. & Wunderlich, J. Antiferromagnetic spintronics. *Nat. Nanotechnol.* **11**, 231–241 (2016).
- Wan, X., Turner, A. M., Vishwanath, A. & Savrasov, S. Y. Topological semimetal and Fermi-arc surface states in the electronic structure of pyrochlore iridates. *Phys. Rev. B* **83**, 205101 (2011).
- Burkov, A. A. & Balents, L. Weyl semimetal in a topological insulator multilayer. *Phys. Rev. Lett.* **107**, 127205 (2011).
- Liu, D. F. et al. Magnetic Weyl semimetal phase in a Kagome crystal. *Science* **365**, 1282–1285 (2019).
- Li, J. et al. Intrinsic magnetic topological insulators in van der Waals layered MnBi_2Te_4 -family materials. *Sci. Adv.* **5**, eaaw5685 (2019).
- Varnava, N. & Vanderbilt, D. Surfaces of axion insulators. *Phys. Rev. B* **98**, 245117 (2018).
- Zhang, R.-X., Wu, F. & Sarma, S. D. “Möbius insulator and higher-order topology in $\text{MnBi}_{2n}\text{Te}_{3n+1}$ ”. *Phys. Rev. Lett.* **124**, 136407 (2020).
- Marti, X. et al. Room-temperature antiferromagnetic memory resistor. *Nat. Mater.* **13**, 367–374 (2014).
- Wadley, P. et al. Electrical switching of an antiferromagnet. *Science* **351**, 587–590 (2016).
- Kirilyuk, A., Kimel, A. V., & Rasing, T. Ultrafast optical manipulation of magnetic order. *Rev. Mod. Phys.* **82**, 2731–2784 (2010).
- Tzschaschel, C. et al. Ultrafast optical excitation of coherent magnons in antiferromagnetic NiO. *Phys. Rev. B* **95**, 174407 (2017).
- Kampfrath, T. et al. Coherent terahertz control of antiferromagnetic spin waves. *Nat. Photon.* **5**, 31–34 (2011).
- Pashkin, A., Sell, A., Kampfrath, T. & Huber, R. Electric and magnetic terahertz nonlinearities resolved on the sub-cycle scale. *N. J. Phys.* **15**, 065003 (2013).
- Suzuki, M. T., Koretsune, T., Ochi, M. & Arita, R. Cluster multipole theory for anomalous Hall effect in antiferromagnets. *Phys. Rev. B* **95**, 094406 (2017).
- Nayak, A. K. et al. Large anomalous Hall effect driven by a non-vanishing Berry curvature in the noncolinear antiferromagnet. *Sci. Adv.* **2**, e1501870 (2016).
- Kiyohara, N. et al. Giant anomalous Hall effect in the chiral antiferromagnet Mn_3Ge . *Phys. Rev. Appl.* **5**, 064009 (2016).
- Kim, W. J. et al. Strain engineering of the magnetic multipole moments and anomalous Hall effect in pyrochlore iridate thin films. *Sci. Adv.* **6**, eabb1539 (2020).

22. Higo, T. et al. Large magneto-optical Kerr effect and imaging of magnetic octupole domains in an antiferromagnetic metal. *Nat. Photon* **12**, 73–78 (2018).
23. Kimata, M. et al. Magnetic and magnetic inverse spin Hall effects in a non-collinear antiferromagnet. *Nature* **565**, 627–630 (2019).
24. Muduli, P. K. et al. Evaluation of spin diffusion length and spin Hall angle of the antiferromagnetic Weyl semimetal Mn_3Sn . *Phys. Rev. B* **99**, 184425 (2019).
25. Zhang, Y. et al. Strong anisotropic anomalous Hall effect and spin Hall effect in the chiral antiferromagnetic compounds Mn_3X (X = Ge, Sn, Ga, Ir, Rh, and Pt). *Phys. Rev. B* **95**, 075128 (2017).
26. Ikhlas, M. et al. Large anomalous Nernst effect at room temperature in a chiral antiferromagnet. *Nat. Phys.* **13**, 1085–1090 (2017).
27. Chen, T. et al. Anomalous transport due to Weyl fermions in the chiral antiferromagnets Mn_3X , X = Sn, Ge. *Nat. Commun.* **12**, 572 (2021).
28. Sakai, A. et al. Giant anomalous Nernst effect and quantum-critical scaling in a ferromagnetic semimetal. *Nat. Phys.* **14**, 1119–1124 (2018).
29. Broholm, C. et al. Antichiral spin order, its soft modes, and their hybridization with phonons in the topological semimetal Mn_3Ge . *Phys. Rev. B* **102**, 054403 (2020).
30. Liang, T. et al. Orthogonal magnetization and symmetry breaking in pyrochlore iridate $\text{Eu}_2\text{Ir}_2\text{O}_7$. *Nat. Phys.* **13**, 599–603 (2017).
31. Kimata, M. et al. X-ray study of ferroic octupole order producing anomalous Hall effect. *Nat. Commun.* **12**, 5582 (2021).
32. Zhou, J. et al. Large spin-orbit torque efficiency enhanced by magnetic structure of collinear antiferromagnet IrMn . *Sci. Adv.* **5**, eaau6696 (2019).
33. Tang, H. X. et al. Giant planar Hall effect in epitaxial (Ga, Mn) As devices. *Phys. Rev. Lett.* **90**, 107201 (2003).
34. Bowen, M. et al. Order-driven contribution to the planar Hall effect in Fe_3Si thin films. *Phys. Rev. B* **71**, 172401 (2005).
35. Ge, Z. et al. Magnetization reversal in (Ga, Mn) As/Mn O exchange-biased structures: Investigation by planar Hall effect. *Phys. Rev. B* **75**, 014407 (2007).
36. Bason, Y. et al. Giant planar Hall effect in colossal magnetoresistive $\text{La}_{0.84}\text{Sr}_{0.16}\text{MnO}_3$ thin films. *Appl. Phys. Lett.* **84**, 2593 (2004).
37. Liang, D. et al. Origin of planar Hall effect in type-II Weyl semimetal MoTe_2 . *AIP Adv.* **9**, 055015 (2019).
38. Yang, S. et al. Field-modulated anomalous Hall conductivity and planar Hall effect in $\text{Co}_3\text{Sn}_2\text{S}_2$ nanoflakes. *Nano Lett.* **20**, 7860–7867 (2020).
39. Li, P. et al. Giant planar Hall effect in the Dirac semimetal $\text{ZrTe}_{5-\delta}$. *Phys. Rev. B* **98**, 121108 (2018).
40. Burkov, A. A. Giant planar Hall effect in topological metals. *Phys. Rev. B* **96**, 041110 (2017).
41. Li, Y. et al. Correlated magnetic Weyl semimetal state in strained $\text{Pr}_2\text{Ir}_2\text{O}_7$. *Adv. Mat.* **33**, 2008528 (2021).
42. Huang, D. et al. Planar Hall effect with sixfold oscillations in a Dirac antiperovskite. *Phys. Rev. Res.* **3**, 013268 (2021).
43. Neha, W. et al. Planar Hall effect and anisotropic magnetoresistance in the polar-polar interface of LaVO_3 - KTaO_3 with strong spin-orbit coupling. *Nat. Commun.* **11**, 874 (2020).
44. Bhardwaj, A. et al. Observation of planar Hall effect in topological insulator— Bi_2Te_3 . *Appl. Phys. Lett.* **118**, 241901 (2021).
45. Suzuki, M. T. et al. Multipole expansion for magnetic structures: A generation scheme for a symmetry-adapted orthonormal basis set in the crystallographic point group. *Phys. Rev. B* **99**, 174407 (2019).
46. Tian, Z. et al. Field-induced quantum metal-insulator transition in the pyrochlore iridate $\text{Nd}_2\text{Ir}_2\text{O}_7$. *Nat. Phys.* **12**, 134 (2016).
47. Kuroda, K. et al. Evidence for magnetic Weyl fermions in a correlated metal. *Nat. Mater.* **16**, 1090–1095 (2017).
48. Li, X. et al. Chiral domain walls of Mn_3Sn and their memory. *Nat. Commun.* **10**, 3021 (2019).
49. You, Y. et al. Cluster magnetic octupole induced out-of-plane spin polarization in antiperovskite antiferromagnet. *Nat. Commun.* **12**, 6524 (2021).
50. Xu, L. et al. Planar Hall effect caused by the memory of antiferromagnetic domain walls in Mn_3Ge . *Appl. Phys. Lett.* **117**, 222403 (2020).
51. Witczak-Krempa, W., Go, A. & Kim, Y. B. Pyrochlore electrons under pressure, heat, and field: Shedding light on the iridates. *Phys. Rev. B* **87**, 155101 (2013).

Acknowledgements

This work was supported by the Research Center Program of the IBS (Institute for Basic Science) in Korea (grant no. IBS-R009-D1). Y.Z. and Y.L. acknowledge the support provided by the Qilu Young Scholars Program of Shandong University. W.J.K. was supported by the U.S. Department of Energy (DOE), Office of Basic Energy Sciences, Division of Materials Sciences and Engineering (contract No. DE-AC02-76SF00515), and the Gordon and Betty Moore Foundation's Emergent Phenomena in Quantum Systems Initiative (grant No. GBMF9072, synthesis equipment). B.-J.Y. was supported by the Samsung Science and Technology Foundation under Project No. SSTF-BA2002-06 and National Research Foundation of Korea (NRF) Grants funded by the Korean government (MSIT) (No. 2021R1A2C4002773 and No. NRF-2021R1A5A1032996).

Author contributions

J.S. and Y.L. conceived the idea and designed the experiments. T.O. performed the calculation of the orthogonal magnetization effect on the planar Hall effect under the supervision of B.J.Y. J.S. grew and characterized the structure of the samples. J.S., Y.L., Y.Z., E.K., and J.L. performed the magnetotransport measurements. J.S., T.O., W.J.K., B.J.Y., T.W.N., and Y.L. analyzed the results and wrote the manuscript. All authors participated in the discussion during the manuscript preparation.

Competing interests

The authors declare no competing interests.

Additional information

Supplementary information The online version contains supplementary material available at <https://doi.org/10.1038/s41467-022-34189-6>.

Correspondence and requests for materials should be addressed to Yangyang Li or Tae Won Noh.

Peer review information *Nature Communications* thanks the anonymous reviewer(s) for their contribution to the peer review of this work. Peer reviewer reports are available.

Reprints and permissions information is available at <http://www.nature.com/reprints>

Publisher's note Springer Nature remains neutral with regard to jurisdictional claims in published maps and institutional affiliations.

Open Access This article is licensed under a Creative Commons Attribution 4.0 International License, which permits use, sharing, adaptation, distribution and reproduction in any medium or format, as long as you give appropriate credit to the original author(s) and the source, provide a link to the Creative Commons license, and indicate if changes were made. The images or other third party material in this article are included in the article's Creative Commons license, unless indicated otherwise in a credit line to the material. If material is not included in the article's Creative Commons license and your intended use is not permitted by statutory regulation or exceeds the permitted use, you will need to obtain permission directly from the copyright holder. To view a copy of this license, visit <http://creativecommons.org/licenses/by/4.0/>.

© The Author(s) 2022